Targeting hPKM2 in cancer: A bio isosteric approach for ligand design

Ludovico Pipitò [a,*], Thomas Arron Illingworth [b,**], Giuseppe Deganutti [a]

[a] Centre for Sport, Exercise and Life Sciences, Faculty of Health and Life Sciences, Coventry University, Coventry, CV1 5FB, UK
[b] University of Derby, College of Science and Engineering, School of Human Sciences, DE22 1GB, UK

ABSTRACT

The term cancer refers to a plethora of diseases characterized by the development of abnormal cells that divide uncontrollably and can infiltrate further proximal or distal body tissues. Each type of cancer can be defined by aggressiveness, localization, metabolism, and response to available treatments. Among the most common hallmarks of cancer is a more acidic intracellular microenvironment. Offset pH values are due to an excess of lactate and an increased hypoxia-inducible factor (HIF) expression, which leads to a hypoxic state and a metabolic shift towards glycolysis to produce adenosine-5′-triphosphate (ATP) necessary for cellular metabolism. Warburg's hypothesis underpins this concept, making glycolysis and its central enzyme pyruvate kinase (hPKM2), an ideal target for drug development. Using molecular docking and extensive molecular dynamics (MD) simulations we investigated the binding mode of phosphoenolpyruvate (PEP) inside the hPKM2 active site, and then evaluated a set of known bio-isosteric inhibitors to understand the differences caused by their substitutions on their binding mode. Ultimately, we propose a new molecular entity to hamper hPKM2, unbalance cellular energy, and possibly trigger autophagic mechanisms.

1. Introduction

Cancer is characterised by an uncontrolled proliferative capacity [1], driven by genetic and epigenetic alterations of cell functions like metabolism [2], and proliferative and survival pathways. The result is cells that are capable of growing exponentially, impairing tissue and organ function in the process [3]. Cancer cells have higher metabolic outputs compared to healthy cells, which is achieved through over-expression and hyperactivity of various enzymes [2] involved in key metabolic pathways, including glucose uptake and glycolysis [4] to promote a pro–survival environment for cancer. The "Warburg hypothesis" [5] describes the glycolytic metabolic shifts in both aerobic and anaerobic conditions observed within solid-state tumours [6,7], gained through overexpression of glucose transporters, increased ATP production, and lactate accumulation in the tumour microenvironment (TME). Metabolic remodelling of the tumour favours disease progression and impedes treatment opportunities, due in large part to chemotherapy resistance, shifting preference for hypoxic states through lactate-dependent mechanisms to produce ATP in absence of oxygen [8]. The result of this is a survival advantage with respect to energy production, leading to tumour progression, angiogenesis, and metastasis

[9]. Oxygen deficiency also promotes hypoxia-inducible factors (HIF), which in turn over expresses glucose transporter (GLUT1) to facilitate glucose uptake for tumour progression [10]. HIF-1α triggers several tumour-promoting pathways. HIF1α alters lactate dehydrogenase A isoform expression (LDH-A), impacting cellular pH, ion balance, as well as hypoxia response elements linked to cancer progression [11]. Additionally, HIF-1 is involved in the transcription of glycolytic enzymes ultimately linked with metabolic regulators such as the mammalian target of rapamycin (mTOR), through the AMP-activated protein kinase pathway (AMPK 5). This inhibits apoptotic response elements in response to increased concentrations of ATP [10]. Cancers exhibiting a HIF-glycolytic state act within the extracellular space, where interleukin 1 beta (IL-1β) and tumour necrosis factor-alpha (TNF-α) promote an increased expression of pro-inflammatory factors and angiogenesis via HIF-mediated vascular endothelial growth factor (VEGF) overexpression with increased M1 macrophage recruitment [12–14]. It might also restore physiological lactate levels, reducing expression levels of phosphofructokinase 1 (PFK1), histone acetylation, inactivation of p53, and the overexpression of the multi-drug resistance (MDR) factors and genes [15], responsible for drug resistance [16]. In conditions of reduced oxidative phosphorylation and fatty acid oxidation for ATP production,

---

* Corresponding author.
** Corresponding author.
E-mail addresses: pipitol@uni.coventry.ac.uk (L. Pipitò), t.illingworth@derby.ac.uk (T.A. Illingworth), ad5288@coventry.ac.uk (G. Deganutti).

the prominent resource left to sustain the hyperactive cell metabolism is glycolysis, making glycolysis an ideal target for therapeutic approaches [17]. All the interconnected pathways mentioned and their influence on oncogenic phenotype are summarised in Fig. 1.

Pyruvate kinase (hPK) is a rate-limiting glycolysis enzyme, responsible for the irreversible transphosphorylation of a phosphate group from phosphoenolpyruvate (PEP) to adenosine diphosphate (ADP) to produce ATP [18]. There are four human isoforms of PK, encoded by three tissue-specific genes: the L isoform is expressed in the liver, R in erythrocytes, and M in muscles as a result of alternative splicing of exon 9 and 10 (M1 and M2) which differ by 22 positions, located near the allosteric regulation site for 1,6 fructose bisphosphate (FBP) and specific deletions in tumour cells [19]. Human pyruvate kinase M2 (hPKM2) increased level of expression is found in a variety of cancers such as gastric, colorectal, and bile duct, rheumatic diseases, lung cancer, breast cancer, neuroendocrine tumours, urological malignancies, renal cell carcinoma, diabetic nephropathy, haematological malignancies, prostate cancer, and thyroid carcinoma [20]. hPKM2 is expressed in tissues with anabolic functions, including proliferating cells and cancer [21], suggesting that it could be a suitable target in cancer therapy. The development of safe and effective treatments targeting the glycolytic pathway provides an opportunity to interrupt the dysregulated homeostasis observed in cancer. Numerous studies related hPKM2 inhibition with a positive effect on cancer progression [22–26], however the specific mechanism of action is still not fully understood. A promising clinical trial for the hPKM2 inhibitor TLN-232/CAP-232 was conducted by Thallion Pharmaceuticals in 2007 but was terminated due to legal
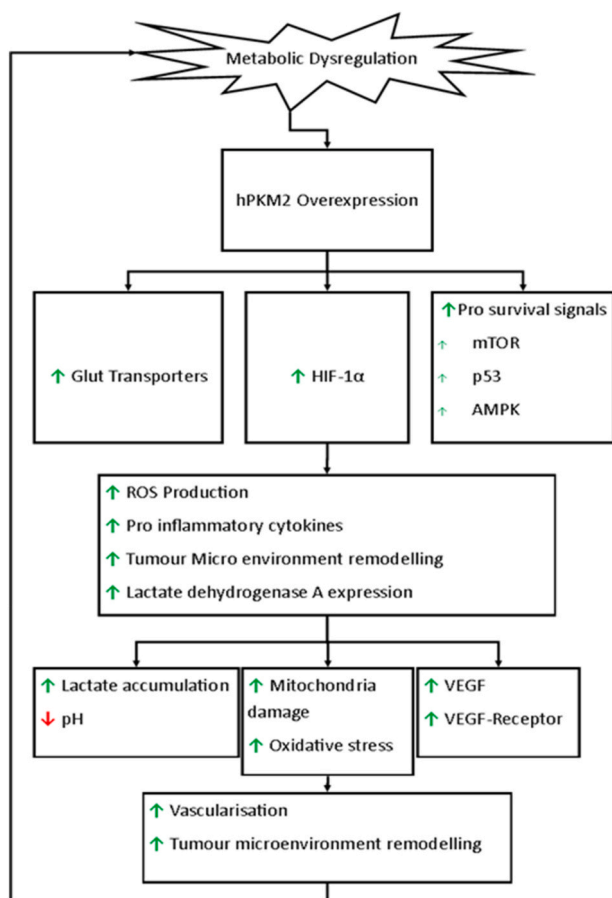

Fig. 1. The central role of hPKM2 in conjunction with metabolic adjustments occurring in oncotic phenotypes. The positive feedback contributes to establishing new pathological homeostasis with distinctive hallmarks which act in TME. The endpoint of all the transformations leads to tumour development and increased therapy resistance, which is linked to poor prognosis.
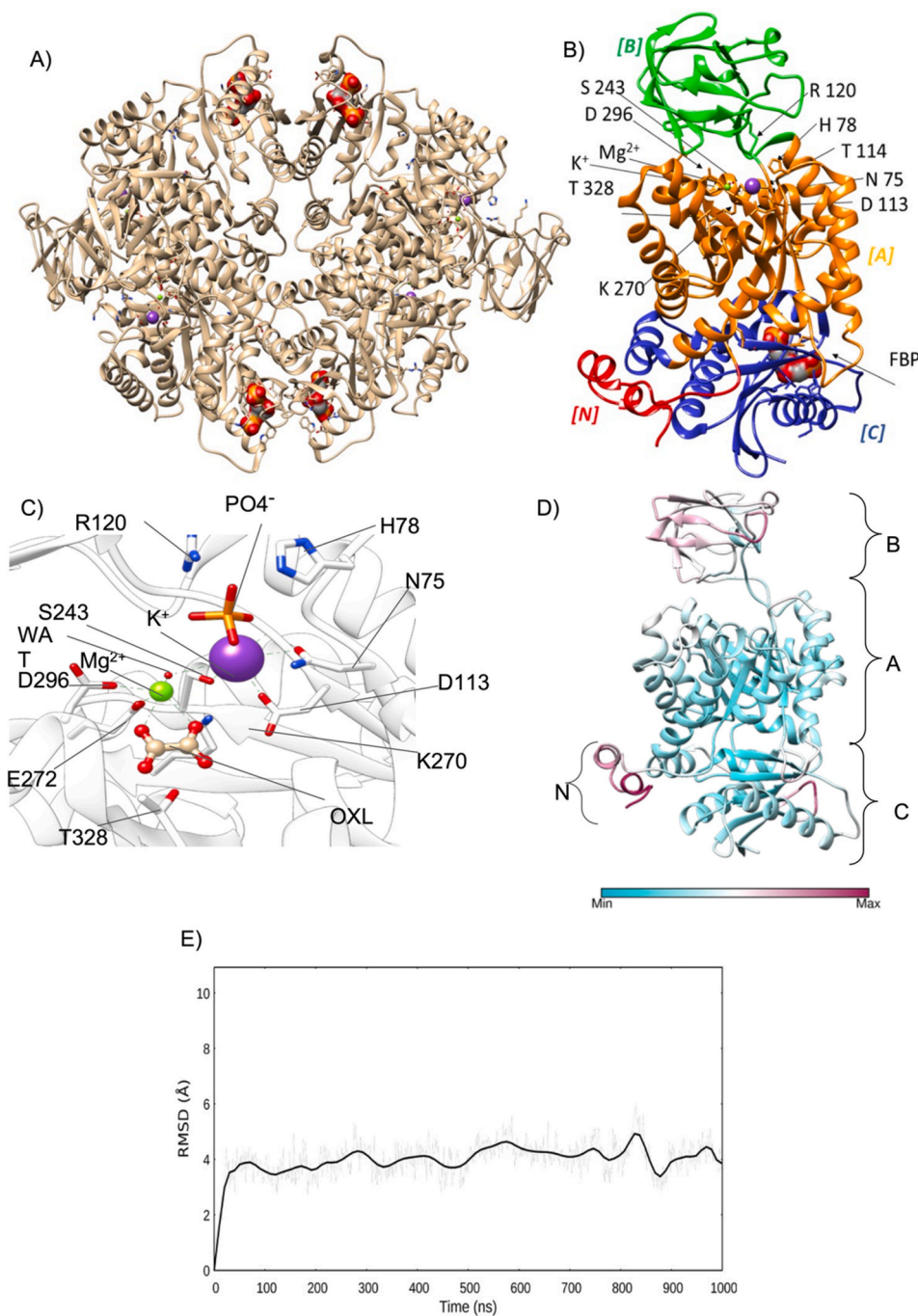
reasons [10]. Shikonin and its analogues have been shown to effectively inhibit hPKM2, demonstrating selectivity for hPKM2 [25–28], impairing the glycolytic pathway for ATP production. Using hPKM2 crystallographic information as a starting point, we employed extensive molecular docking and molecular dynamics (MD) simulations to highlight, for the first time, the binding mode of PEP inside the hPKM2 catalytic site. Additionally, we describe the binding mode for a set of experimentally tested PEP bio-isosteres compounds [29,30], then propose and test *in silico* a modification of the enol moiety of PEP as a bio-isosteric substitution to improve the inhibitors' stability to possibly reduce chemotherapy resistance [27]. We evaluate the binding energy of the compounds with extensive molecular mechanics energy combined Poisson-Boltzmann energy surface area (MM-PBSA). This work reinvigorates the research of small molecules able to inhibit hPKM2, with the aim of depleting cancerous cells of their main ATP source.

2. Methods

2.1. Protein preparation and force field settings

All systems were prepared using the CHARMM36/CGenFF 3.0.1 [31, 32] force field combination. hPKM2 structure tetramer was retrieved from PDB 1T5A [20] and modelled, restricting our system to a single chain. The Na^+ and Mg^{2+} ions were kept, while FBP was removed to study the binding capacity of the enzyme in its unbound pre-activation state, where the Mg^{2+}-ADP complex is not present in the binding site. FBP was not considered, as we aimed to study PEP inside the catalytic site in the pre-catalytic state. The protonation state of residues was calculated by Propka [33] at a simulated pH of 6.5 to match the tumour intracellular pH [34,35], and edited by pdb2pqr [36], while disulfide bonds were identified by HTMD [37], visually inspected, and patched manually through VMD [38]. The protein potential energy was minimised through 1000 steps of the conjugate gradient algorithm using ACEMD [39].

2.2. Ligand preparation and parameter settings

PEP structure (PubChem: 348274362) was built as a template for building all the bio isosteric molecules considered (Fig. 2A, Table 1) using the VMD Molefacture plugin (https://www.ks.uiuc.edu/Research/vmd/plugins/molefacture/) while functional group substitutions or ligand modifications were performed with Chimera [40]. ADMET prediction was computed using ADMETlab 2.0 [41] and included the toxicological profiles (Table S1). Ligand descriptors were calculated with RDkit [42,43]. For each ligand, the initial docking poses and scores were obtained using Autodock Vina [44,45] by centring an isometric grid box on residue K270 with a side of 46 Å. To validate the docking protocol, we performed the self-docking of the only inhibitor with structural information available, oxalacetate (OXL) (PDB entry 1T5A). The OXL self-docking displayed an RMSD of 0.93 Å, suggesting an adequate performance of the docking (Fig. S1F). Results that displayed conformations similar to the X-ray crystallography in terms of the orientation of the phosphate moiety toward the PO_4 group as resolved in 1T5A (Fig. S1) were used as starting coordinates for MD simulations. For each ligand, the initial parameters were obtained through the CGenFF server [46,47]. Atomic charges were calculated with the restrained electrostatic potential (RESP) using the Antechamber package [48], while angles and dihedrals with high penalty scores were optimised using Gaussian 09 [49] using the MP2/6-31g(d) level of theory. All ligands were simulated individually in water in short MDs for a visual evaluation of the reliability of the parameters.

2.3. System preparation for molecular dynamics (MD)

hPKM2 structure and topology files were prepared using VMD's Psfgen plugin (https://www.ks.uiuc.edu/Research/vmd/plugins/
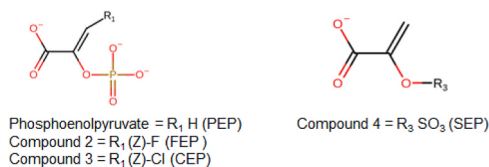
Fig. 2. Crystal structure of hPKM2 and its active site domains. A) The X-ray diffraction structure of tetrameric hPKM2 (PDB 1T5A, tan ribbon) with FBP is represented as a molecular surface in the allosteric pocket. Ions and phosphate are represented as a ball and sticks; **B)** closeup ribbon representation of hPKM2 monomer with domain classification is shown [62]: the N-terminal domain (residues I13-A42 in red), the A domain hosting the binding site where ions are present (residues R43-K115, K224-A387), the B domain (G116-E223), and C domain (A388-P531). **C)** Single chain closeup ribbon structure of hPKM2 monomer in complex with OXL. The OXL position is stabilized by the Mg^{2+} ion which is suggested to support the phosphoryl transition. A phosphate group is shown as a ball and stick to indicate where the Mg^{2+} - ADP should be **D)** RMSF values plotted on the ribbon representation of hPKM2 with domains classification: N-terminal domain (residues I13-A42), the A domain hosting the binding (residues R43-K115, K224-A387), the B domain (G116-E223), and C domain (A388-P531). **E)** RMSDs of hPKM2 alpha carbon atoms over time, which averaged 3.9 ± 0.63 Å, indicating that the monomer remained stable.

psfgen/), and the resulting structures were visually inspected. The systems were simulated for a total time of 1000 ns with TIP3P water molecules [51] added to the simulation box using the Solvate plugin 1.5 (http://www.ks.uiuc.edu/Research/vmd/plugins/solvate/) to give a 10 Å padding in every direction. The charge neutrality was achieved by adding Na^+/Cl^- to the concentration of 0.150 M using the Autoionize plugin 1.3 (http://www.ks.uiuc.edu/Research/vmd/plugins/autoionize/). ACEMD was used for both the equilibration and the productive MD trajectories. The energy of the systems was reduced through 1000 conjugate-gradient minimization steps to eliminate possible clashes and optimize atomic distances. Equilibration was reached in isothermal-isobaric conditions (NPT) using the Berendsen barostat [52] (target pressure 1 atm) and the Langevin thermostat [53] (target temperature 310 K) during a 4 ns long MD simulation (integration time step

2 fs). During the equilibration, a positional restraint of 1 kcal/mol $Å^2$ was applied on the alpha carbons of hPKM2 for the first 3 ns, while ligands' restraints were kept through the whole equilibration to avoid unwanted displacements. Positional restraints of 1 kcal/mol $Å^2$ were also applied on protein side chains for the first 2 ns. Productive trajectories were produced with an integration time step of 4 fs, using hydrogen mass repartition [54] in the canonical ensemble (NVT), with no positional restraints. The cut-off distance for electrostatic interactions was set at 9 Å, with a switching function applied beyond 7.5 Å. Long-range Coulomb interactions were handled using the particle mesh Ewald summation method (PME) [55] with default ACEMD settings.

Table 1

List of hPKM2 inhibitors.

Phosphoenolpyruvate = R_1 H (PEP)
Compound 2 = R_1 (Z)-F (FEP)
Compound 3 = R_1 (Z)-Cl (CEP)

Compound 4 = R_3 SO_3 (SEP)

Name	Molecular Weight (Da)	pK$_d$ or pIC$_{50}$
PEP	164.96	5.6 [1]
Compound 2	182.92	7 [2]
Compound 3	198.92	7.3 [2]
Compound 4	165.95	2.3 [2]

The table above shows the different functional group addition and modifications as experimentally performed by Garcìa-Alles et al. [29].

[1] Experimental pK$_d$ reported by Duffy et al. [50].
[2] pIC$_{50}$ as reported by Garcìa-Alles et al. [29].

2.4. MD trajectories analysis

The root mean square deviation (RMSD) and root mean square fluctuation (RMSF) analyses were computed using VMD and MDTraj [56]. Ligand-protein contacts, including hydrogen bonds, were detected using the GetContacts scripts tool (https://getcontacts.github.io), with a threshold distance and angle of 3.5 Å and 120°, respectively. Contacts and HB were expressed as occupancy (% of total MD frames). The Molecular Mechanics Poisson-Boltzmann Surface Area (MMPBSA) was computed with the MMPBSA.py [57–59] script (AmberTools20 suite at http://ambermd.org/), converting the CHARMM psf topology files to Amber prmtop format through ParmEd (http://parmed.github.io/ParmEd/html/index.html).

3. Results

3.1. Assessing the dynamics of apo hPKM2

The X-ray diffraction structure of hPKM2 (PDB: 1T5A) reports the tetrameric hPKM2 (Fig. 2A) in complex with the inhibitor oxalate (OXL) and the positive allosteric modulator FBP. hPKM2 forms a tetrameric structure through the C and N domains, while the catalytic site is situated between the A and B domains (Fig. 2B). In the catalytic site of each monomer, OXL engages T328 and K270 side chains in hydrogen bonds and forms bidentate coordination with an Mg^{2+} ion, which in turn coordinates with D296, E272, and a water molecule (Fig. 2C). A potassium ion occupies the inner part of the pocket, coordinating with the former water molecule and S243, D113, N75, and T114 (backbone). Situated in a more external site between the A and B domains [20], a phosphate group interacts with R120 and H78, in correspondence with the site putatively occupied by ADP (Fig. 2C).

During a 1μs MD simulation, the extremities of domains N and B exhibited the highest flexibility (Fig. 2D), in line with previous work [60]. We assessed the dynamics of the apo hPKM2 (obtained by removing OXL and FBP) by measuring the RMSD to 1T5A (Fig. 2E), which resulted in 2.8 ± 0.9 Å, in agreement with the nominal resolution (2.8 Å) of 1T5A. The flexibility displayed by the FBP pocket indicated that this site is stabilized by the allosteric modulator. The catalytic site residues S243, T114, and D113 oriented their sidechains toward K270 and remained stable throughout the simulation (Video S1). Intriguingly, the Mg^{2+} ion remained interlocked between D296 and E272, in line with its crucial role in coordinating the substrate binding as well as the catalytic mechanism [20]. The catalytic residues are encompassed between domain A and the mobile domain B which has been reported to close in the presence of Mg^{2+}, ADP [18], and K$^+$. We did not observe any spontaneous closing of the B domain onto the A domain, due to the

absence of the Mg^{2+}-ADP complex connecting the two domains [61]. However, the residues R73, K270, S240, D113, T114, E272, and D296, involved in the enzymatic reaction, kept their original orientation during the simulation, indicating minimal conformational changes.

Taken together, these results indicate that, the stability of the catalytic site is secured by the tight inter-residue network of contacts and hydrogen bonds and suggest that the catalytic site could be a template for the structure-based drug design of novel inhibitors, in the absence of the FBP from the allosteric site. Although the potassium ion may be present in the ground state hPKM2 [61], it was soon displaced in the absence of the stabilizing substrate, while the Mg^{2+} was completely and independently stabilized by the D296 and E272 active site residues, suggesting that Mg^{2+} should be considered for drug design purposes.

3.2. Phosphoenolpyruvate binding mode

Although the catalytic mechanism of PKM2 is well known, to the best of our knowledge no information is available about PEP interactions within the active site, as there are no reported structural or computational studies addressing the binding mode of PEP before its phosphate group is transferred to ADP (pre-catalytic state). To tackle this knowledge gap, we docked PEP to hPKM2 and performed post-docking MD simulation. PEP was overall stable throughout the MD trajectory (RMSD = 2.31 ± 0.47 Å, Fig. S2A, RMSF = 2.09 ± 0.63 Å Fig. S2B) although it completely stabilized in the second half of the simulations thanks to the coordination of Na+ and Mg^{2+} ions by the carboxylic and phosphate groups, with the aid of D178, E272, and D296 to complete the coordination (Video S2). Contacts and hydrogen bonds analysis between PEP and the hPKM2 active site (Fig. 3) highlights the interaction of the PEP phosphate group with the Mg^{2+}ion corroborating the crucial role of the cation in coordinating PEP, as previously reported [20][61]. M291 and T328 directly engaged the enol pyruvate in interatomic contacts, while R73 and K270 formed hydrogen bonds with PEP carboxyl moiety (Fig. 3A, Video S2). The MM-PBSA calculated binding free energy for compound 2 was −52.98 ± 23.08 kcal/mol, with E272 and D296 being the major contributors to the stability (Fig. S3).The stability of PEP during the MD simulation suggests that this is the binding mode the substrate adopts in the pre-catalytic hPKM2. We identified a set of interactions that stabilize PEP within the catalytic site. A network of hydrogen bonds is formed between the carboxyl group of PEP and R73 and K270. D178 interacts with the phosphate group through the Na$^+$ ion, while E272 and D296 engaged the phosphate group through the Mg^{2+} ion, locking the orientation of the phosphate toward E272 and D296 while orienting the carboxyl group toward K115 and R120 (Fig. 3B).

3.3. Halogenated PEP-derivatives are stable in the catalytic site

As previously reported by Garcìa-Alles et al. [29], the modification of the phosphate or the carboxylate groups reduces the binding affinity of PEP bio-isosteres toward hPKM2, suggesting these moieties as crucial for binding, in accordance with our MD simulation of PEP. Compounds 2 and 3 (Table 1) bear both the carboxylate and phosphate with the addition of a halogen atom on the ethylene scaffold to deactivate the substrate thanks to an electronic effect. hPKM2 possesses Z-stereoselectivity for halogenated PEP-analogue inhibitors such as the (Z)-phosphoenol-3-fluoropyruvate (compound 2) and (Z)-phosphoenol-3-chloropyruvate (compound 3) [50,63]. While fluorinated PEP derivatives inhibit the phosphotransferase reaction, the chlorinated counterparts have a modest effect. As the binding mode of these PEP derivatives s have not been described yet, we investigated their mechanism of action.

3.4. Compounds 2 and 3 binding mode

Compounds 2 and 3 molecular docking results showed both the phosphate group and the scaffold orientation in line with the X-ray
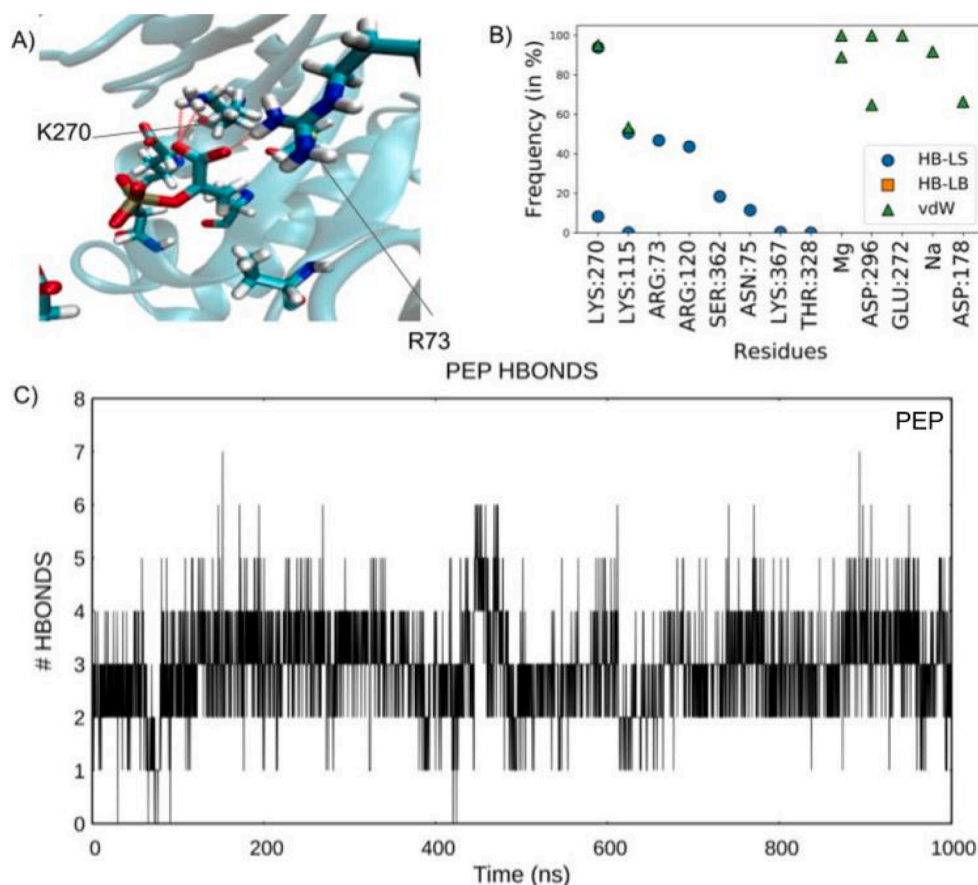
Fig. 3. PEP Binding Site, RMSD, and Hydrogen Bond Network. A) PEP forms a hydrogen bond network throughout the simulation mainly with R73 and K270 (ions not shown) **B)** Contacts occupancy between PEP and hPKM2 are shown with the chain identifier, the residue name, and its number. The double vdW interactions for Mg^{2+} and D296 are due to individual interaction with each oxygen atom of the PEP phosphate group. PEP engaged with a Na^+ ion through the phosphate group. No contact with the ligand's backbone was made during the simulation. C) hydrogen bond count during the simulation (2.93 ± 0.88). HB-LS: hydrogen bond between the ligand and the protein's sidechain; HB-LB: hydrogen bonds between the ligand and the protein's backbone alpha carbon atoms. vdW: ligand-protein interatomic contacts.

structure. (Figs. S1B and S1C). In the best binding pose, the fluorine atom of compound 2 was predicted between E272 and D296, while the carboxyl group oriented towards residue T238 and the phosphate group towards the position occupied by the potassium ion in the X-ray structure. Compound 2 established a set of hydrogen bond interactions with R73, K115, K270, and S362 (Fig. 4A). Post-docking MD simulation displayed stabilizing interactions with residues K73, S362, K115, K270, T328, R120, T175, and E272 (Fig. 4B). During the second half of the MD simulation, compound 2 rearranged within the active site S362 (Video S3) to remain in a stable configuration (RMSD of 2.8 ± 0.91 Å, RMSF of 2.1 ± 0.41 Å Fig. S2A, Fig. S2B respectively). The MM-PBSA computed binding affinity of compound 2 was -53.41 ± 18.6 kcal/mol, with R73 and K270 providing the best interactions (Fig. S4). Compound 3 molecular docking predicted a divergent binding mode compared to compound 2, probably due to the bulkier chlorine atom. The phosphate group engaged R73, K270 and S362 through a set of hydrogen bonds for the totality of the simulation (Fig. 4C), while the carboxyl group coordinated with the Mg^{2+} ion along with E272 and D296. During the simulation, the chlorine atom position varied between A293, M291, and M360 (Video S3) with the molecule being in a stable position between residues R73, K270, S362, K115, D296, E272, M291, T328, A293, and A327 (Fig. 4D), displaying a similar set of interactions as PEP (Fig. 3B).

Despite the relative mobility of compound 3 (average RMSD of 2.51 ± 0.5 Å and average RMSF of 1.4 ± 0.16 Å, Figs. S2A and S2B respectively), the MM-PBSA binding energy was -84.99 ± 9.5 kcal/mol, with R73, R120, K270, and K367 contributing the most to the binding affinity (Fig. S5). Compound 3 phosphate engaged with K270, R73, and S362, suggesting the crucial role of this group in the binding mechanism (Fig. 4C). Compound 3 differed from compound 2 by the stability of the scaffold, locked between R73, K270, M291, E272, and D296. For both compounds, Mg^{2+} and Na^+ ions interacted with the phosphate group

favoring the orientation of the ligand inside the catalytic site (Video S3).

In summary, the presence of the phosphate and the carboxyl groups is required to achieve favorable coordination of the ligands inside the active site. PEP and compound 2 engaged in a similar set of interactions, while compound 3 probably has a different binding mode, although still effective in inhibiting hPKM2 (Table 1) Overall, the shared scaffold between compounds 2, compound 3, and PEP favored a similar stabilizing network of hydrophobic and hydrogen bond interactions.

3.5. A sulfate moiety alters the binding mode within hPKM2

Compound 4 activity was the lowest of all the compounds tested (Table 1). The reason for this is that hPKM2 can still catalyse the sulfonyl transfer from the solfoenolpyruvate (compound 4) to ADP to yield adenosine 5′-sulfatopyrophosphate, with a 250–600 fold reduced reaction rate compared to PEP [64]. Compound 4 best docking pose (Fig. S1 D) was used for post-docking MD simulation, which highlighted a diverged interaction fingerprint from PEP, although still comprising residues R73, K270, S362, T328, and D296, E272 through the Mg^{2+} ion (Fig. 5A). In contrast to PEP, compound 4 engaged R73 and K270 through the carboxyl group for the first 600 ns of the simulation, while the sulfate moiety transitorily interacted with R73 and S362 (Video S3).

The subsequent sulfate displacement from the Mg^{2+} ion briefly produced a rearrangement of the scaffold orientation as indicated by the RMSD (RMSD = 2.18 ± 0.69 Å, RMSF = 1.83 ± 0.35 Å Figs. S2A and S2B). The scaffold reverted to the original position with the sulfate group oscillating between R73 and S362. Compound 4 established a bidentate hydrogen bond interaction with R73 with the sulfate and the carboxyl group, which established a hydrogen bond also with K270. S362 engaged with the sulfate group, while on the other side of the compound, the carboxyl group coordinated with the Mg^{2+} along with
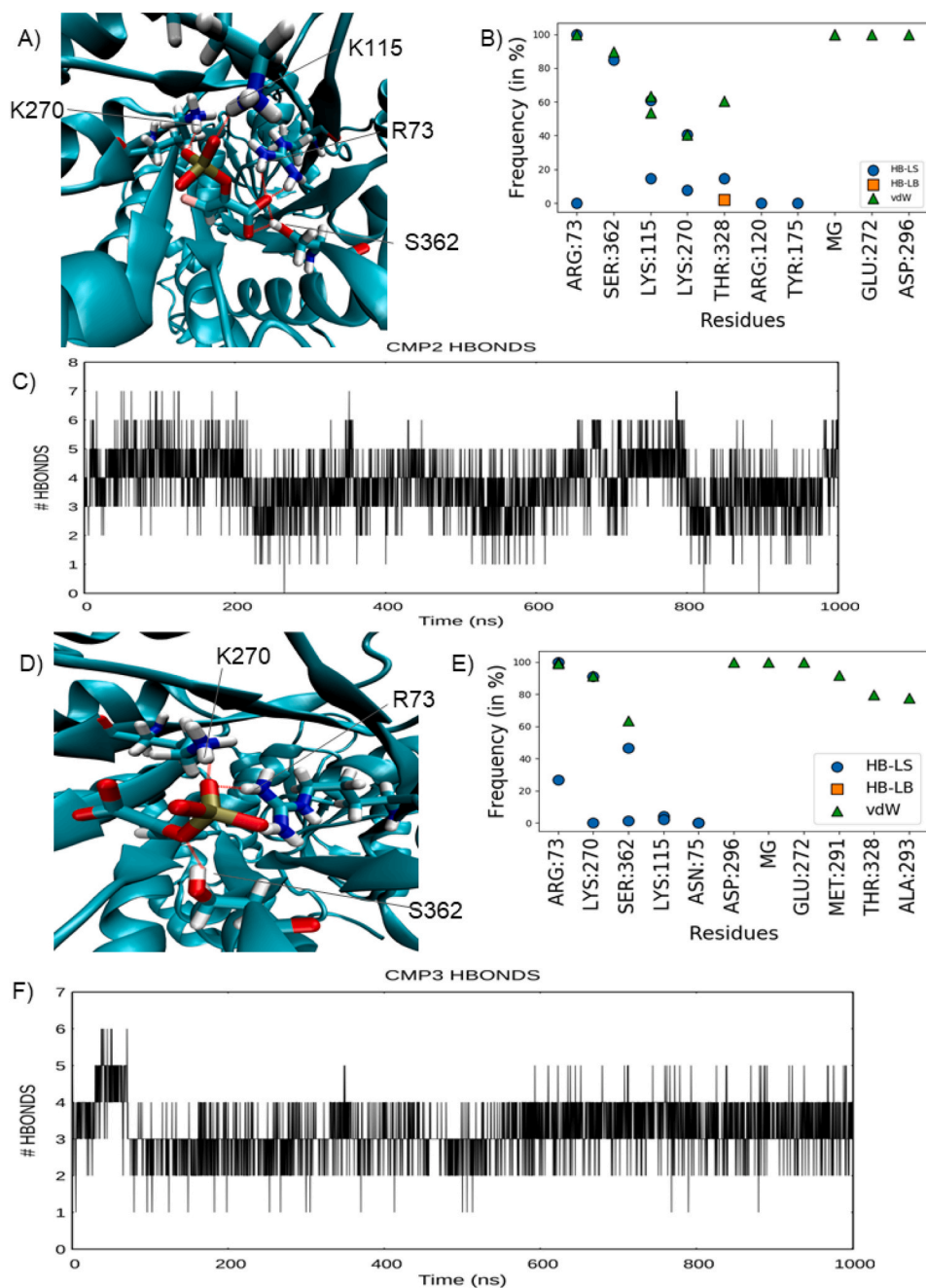
Fig. 4. Compound 2 and Compound 3 Binding Analyses. A) Hydrogen bond network representation of compound 2. Ions are not shown for clarity **B)** Contact plot of compound 2 **C)** Compound 2 hydrogen bond formation plot over time shows an average of 3.8 ± 1.03 bonds **D)** Hydrogen bond network representation of compound 3. Ions are not shown for clarity. **E)** Contact plot of compound 3. **F)** Compound 3 hydrogen bonds count over simulation (3.2 ± 0.63). HB-LS: hydrogen bond between the ligand and the protein's sidechain; HB-LB: hydrogen bonds between the ligand and the protein's backbone alpha carbon atoms. vdW: ligand-protein interatomic contacts.

E272 and D296 (Fig. 5A). The PBSA binding energy for compound 4 was −37.85 ± 6.3 kcal/mol, in line with its modest pIC$_{50}$ (Table 1, Fig. S6).

In summary, compound 4 displayed a different binding mode compared to PEP (Video S3) although engaged the same set of residues as PEP, as the PEP phosphate interactions (i.e., the chelation of the Mg^{2+}) were sustained by compound 4 carboxyl group.

3.6. Extended bio isosteres expand residue engagement in hPKM2 binding site

Our previous simulations highlighted the importance of both the carboxyl and phosphate groups for hPKM2 binding. The ethylene moiety of the scaffold did not engage significantly with any residue, suggesting that modifications or extensions on the scaffold could improve the binding. In addition, the presence of halogen atoms in compounds 2 and 3 negatively impacted the hepatotoxicity profile of the molecules [65,

66], suggesting potential liver injury and poor clearance (1.865 ml/min/Kg and 1.773 ml/min/Kg). Compound 4 was presented with a better ADMET profile, sharing, however, a poor estimated clearance rate (1.896 ml/min/Kg) (Table S1, ADMET Supplementary Information). We, therefore, replaced the halogen atom in compounds 2 and 3 with a primary amide (Compound 5, Table 2) and docked it within the enzyme (Fig. S1E).

During a post-docking MD simulation, compound 5 resided in the active site of hPKM2, resembling PEP interactions and binding mode. The carboxyl group engaged with R73, S362, K270, K115, T328, E272, and D296 (Fig. 6A) locking the scaffold in a favorable orientation inside the active site. An Mg^{2+} cation coordinated both the phosphate and the carbonyl oxygen of the secondary amide, with D296 and E272, further stabilizing the ligand (Video S4). The secondary amide contributed to the stabilization and orientation of the scaffold toward T328. This suggests that additional extensions of compound 5 which include T328
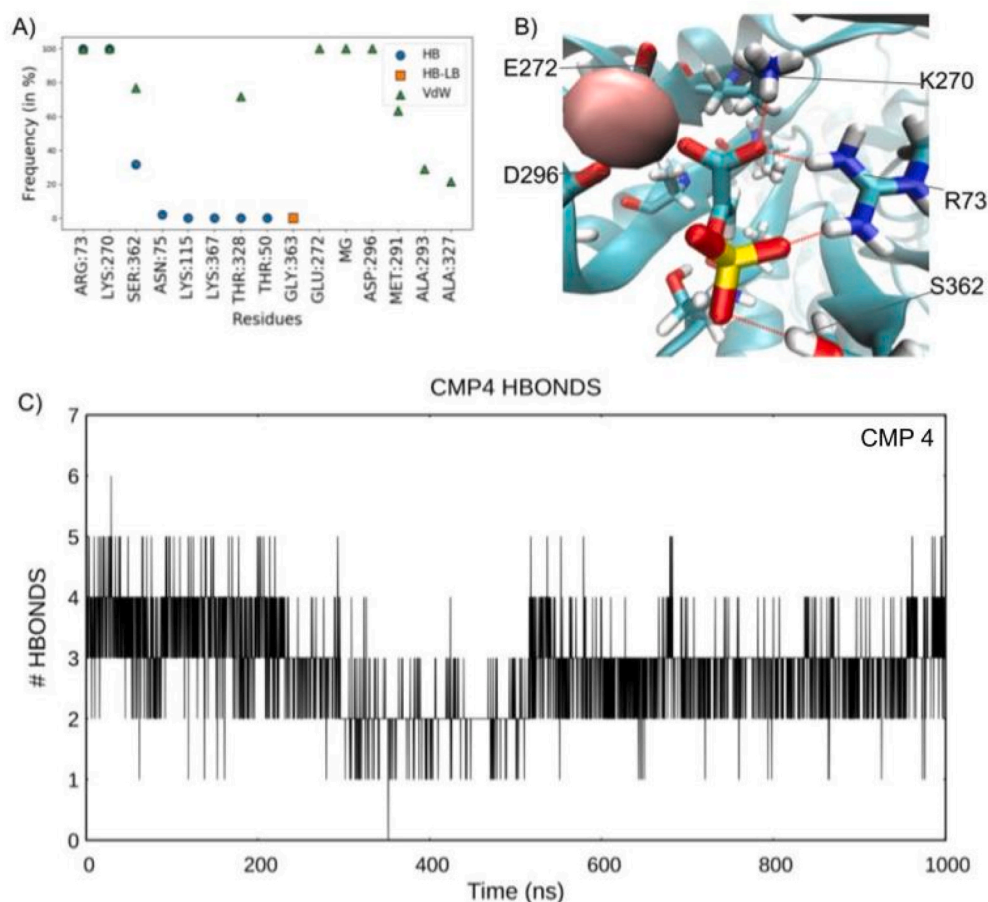
Fig. 5. Compound 4 Binding Mode. A) Contact plot of compound 4 indicates a similar set of interactions with PEP, especially with R73, K270, and T328 **B)** Hydrogen bond network representation of compound 4. C) Compound 4 hydrogen bond count (2.84 ± 0.76) throughout the simulation. HB-LS: hydrogen bond between the ligand and the protein's sidechain; HB-LB: hydrogen bonds between the ligand and the protein's backbone alpha carbon atoms. vdW: ligand-protein interatomic contacts.

Table 2
Proposed Substitution.

Compound 5 = R₅ CONH₂
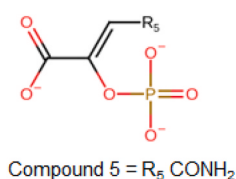
Name	Molecular Weight (Da)	cLogP
Compound 5	207.96	−0.7016

target residue, might be well-tolerated, as indicated by the computed binding energy for compound 5 of −79.36 ± 6.78 kcal/mol, with numerous sets of residues involved in the binding interaction such as R73, K115, R120, K207, K270 and K367 (Fig. S7). Compound 5 (RMSD = 2.96 ± 0.69 Å RMSF = 2.45 ± 0.41 Å, Figs. S2A and S2B), displayed a similar set of hydrogen as PEP (Video S4), with R73, K115, K270, T328, and S362 (Fig. 6B).

Taken altogether, these results confirm the necessity of negatively charged groups (i.e., carboxylate or phosphate) to participate in the coordination of Mg^{2+} by E272 and D296. The presence of the phosphate group with the addition of a secondary amide on the enol pyruvate scaffold contributed to the stabilization of the ligand in accordance with PEP binding mode, with the addition of an improved set of hydrogen bonds and hydrophobic interactions. Furthermore, the ADMET profile of compound 5 indicated no risk of liver injury and an overall safer

toxicology profile including the carcinogenicity output (Table S1, ADMET Supplementary Information).

4. Discussion

The impact of aerobic glycolysis in cancer cells remains one of the hallmarks of cancers. The metabolic shift that sustains the unregulated proliferative capabilities of cancerous cells suggests the main role of hPKM2 in unregulated ATP production. In concert with HIF-1 α expression, an increased hPKM2 activity favours a glycolytic state compared to the oxidative phosphorylation in the cancerous hypoxic TME. The increased glucose uptake with the biochemical pathway shifts initiates a signalling cascade that gives glycolytic cancer types an energetic advantage over regular cells as well as increasing chemotherapeutic resistance. Targeting the overexpressed hPKM2 is a viable, yet scarcely explored therapeutic approach to impact a large variety of cancers. Disrupting the glycolytic ATP production might result in a consistent energy depletion for hypoxic ATP-dependant cancerous cells, thus reducing cell replication rate and possibly causing the activation of the autophagic biochemical pathway. Furthermore, considering the hPKM2 role in drug resistance, the combined hPKM2 inhibition in conjunction with a chemotherapic regime might favour tumour regression with a combined effect derived from ATP depletion, autophagic mechanism, and a reduction in chemotherapy resistance. Disrupting the final irreversible limiting-step of the glycolytic pathway could trigger selective damage to the highly glucose-dependant cancerous cells while having a lower effect on healthy tissues that mainly rely on oxidative phosphorylation.

We provided for the first time insights on the binding mode of PEP within the hPKM2 catalytic site and rationalised the activity of bio-
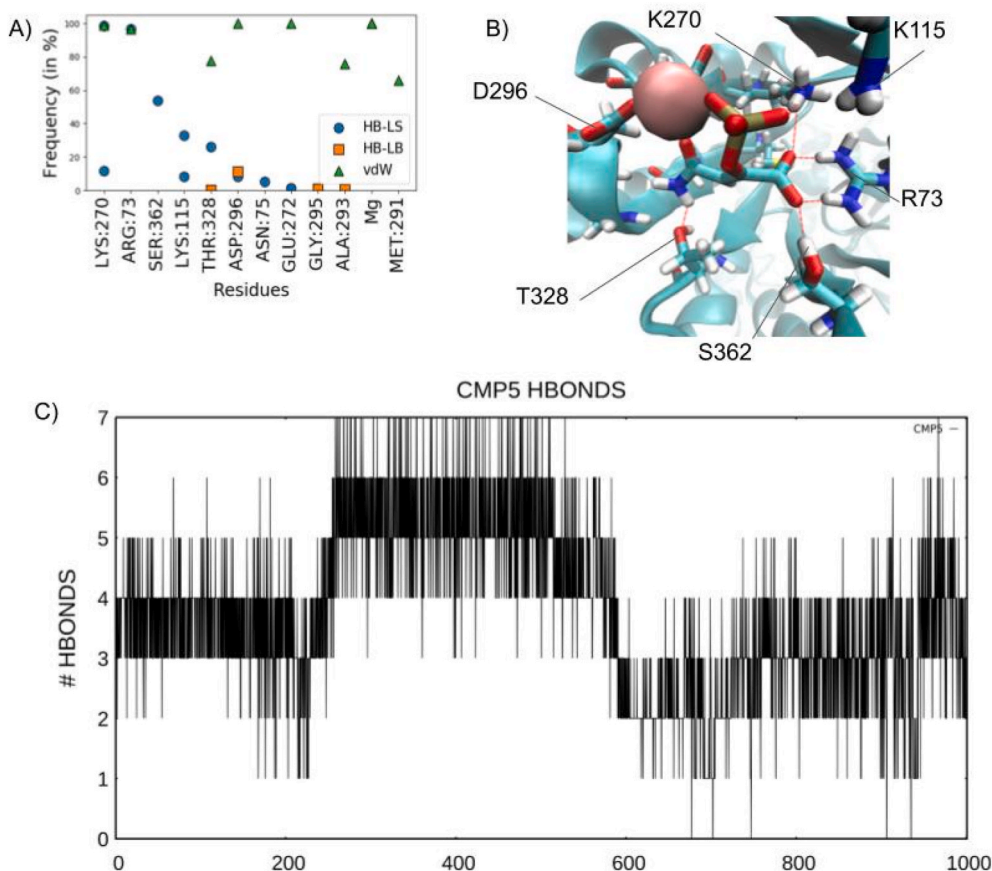
Fig. 6. Compound 5 Binding Mode. A) Contact plot of compound 5 **B)** Hydrogen bond network representation of compound 5. C) Hydrogen bond count (3.76 ± 1.33) over the simulation time. HB-LS: hydrogen bond between the ligand and the protein's sidechain; HB-LB: hydrogen bonds between the ligand and the protein's backbone alpha carbon atoms. vdW: ligand-protein interatomic contacts.

isosteres compounds. The co-presence of the phosphate and carboxyl groups plays an essential function in the orientation of the scaffold by chelating the Mg^{2+} ion, stabilizing the ligand inside the active site. With compound 5, we aimed to design a PEP isostere by keeping the carboxyl and the phosphate groups, crucial elements for enzyme-ligand molecular recognition, expanding the set of interactions between the compound and the active site. We also built the new molecule with no halogen atoms, considering their modest inhibitory impact, improving also the predicted toxicological profile of the molecule. As expected, compound 5 displayed a stable simulated binding mode against hPKM2. We believe it is possible to design new and more potent inhibitors based on compound 5, in which the primary amide is substituted to grow in the catalytic site and form further interactions, besides increasing the drug-likeness of the compounds.

5. Conclusion

We reinforce the potential of the bio-isosteric approach to developing new inhibitors to reduce hPKM2 activity in glycolytic cancer types. Further studies are required to expand on this current work and explore the chemical space of PEP analogues, as well as experimental data to validate our hypothesis.

Declaration of competing interest

The authors declare that they have no known competing financial interests or personal relationships that could have appeared to influence the work reported in this paper.

Appendix A. Supplementary data

Supplementary data to this article can be found online at https://doi.org/10.1016/j.compbiomed.2023.106852.

References

[1] D. Hanahan, R.A. Weinberg, Hallmarks of cancer: the next generation, Cell 144 (2011) 646–674.
[2] V. Fritz, L. Fajas, Metabolism and cancer share common regulatory pathways in cancer cells, Oncogene 29 (2010) 4369–4377.
[3] I.M. Ghobrial, T.E. Witzig, A.A. Adjei, Targeting apoptosis pathways in cancer therapy, CA Cancer J. Clin. 55 (2005) 178–194.
[4] S. Ganapathy-Kanniappan, J.-F.H. Geschwind, Tumor glycolysis as a target for cancer therapy: progress and prospects, Mol. Cancer 12 (2013) 152.
[5] O. Warburg, On the origin of cancer cells, Science 123 (1956) 309–314.
[6] L. Schwartz, C.T. Supuran, K.O. Alfarouk, The warburg effect and the hallmarks of cancer, Anti Cancer Agents Med. Chem. 17 (2017) 164–170.
[7] M.V. Liberti, J.W. Locasale, The warburg effect: how does it benefit cancer cells? Trends Biochem. Sci. 41 (2016) 211–218.
[8] P. Vaupel, H. Schmidberger, A. Mayer, The Warburg effect: essential part of metabolic reprogramming and central contributor to cancer progression, Int. J. Radiat. Biol. 95 (2019) 912–919.
[9] B. Muz, P. de la Puente, F. Azab, A.K. Azab, The role of hypoxia in cancer progression, angiogenesis, metastasis, and resistance to therapy, Hypoxia 3 (2015) 83–92.
[10] K.S. Gill, et al., Glycolysis inhibition as a cancer treatment and its role in an anti-tumour immune response, Biochim. Biophys. Acta 1866 (2016) 87–105.
[11] Y. Hayashi, A. Yokota, H. Harada, G. Huang, Hypoxia/pseudohypoxia-mediated activation of hypoxia-inducible factor-1α in cancer, Cancer Sci. 110 (2019) 1510–1517.
[12] F. Hirschhaeuser, U.G.A. Sattler, W. Mueller-Klieser, Lactate: a metabolic key player in cancer, Cancer Res. 71 (2011) 6921–6925.
[13] I. San-Millán, G.A. Brooks, Reexamining cancer metabolism: lactate production for carcinogenesis could be the purpose and explanation of the Warburg Effect, Carcinogenesis 38 (2017) 119–133.

[14] M. Ying, et al., Lactate and glutamine support NADPH generation in cancer cells under glucose deprived conditions, Redox Biol. 46 (2021), 102065.
[15] K. Bukowski, M. Kciuk, R. Kontek, Mechanisms of multidrug resistance in cancer chemotherapy, Int. J. Mol. Sci. 21 (2020).
[16] P. Icard, L. Fournel, Z. Wu, M. Alifano, H. Lincet, Interconnection between metabolism and cell cycle in cancer, Trends Biochem. Sci. 44 (2019) 490–501.
[17] M.L. Macheda, S. Rogers, J.D. Best, Molecular and cellular regulation of glucose transporter (GLUT) proteins in cancer, J. Cell. Physiol. 202 (2005) 654–662.
[18] W.J. Israelsen, M.G. Vander Heiden, Pyruvate kinase: function, regulation and role in cancer, Semin. Cell Dev. Biol. 43 (2015) 43–51.
[19] W.J. Israelsen, et al., PKM2 isoform-specific deletion reveals a differential requirement for pyruvate kinase in tumor cells, Cell 155 (2013) 397–409.
[20] J.D. Dombrauckas, B.D. Santarsiero, A.D. Mesecar, Structural basis for tumor pyruvate kinase M2 allosteric regulation and catalysis, Biochemistry 44 (2005) 9417–9429.
[21] C.V. Dang, PKM2 tyrosine phosphorylation and glutamine metabolism signal a different view of the Warburg effect, Sci. Signal. 2 (2009) pe75.
[22] J.H. Park, et al., Specific pyruvate kinase M2 inhibitor, compound 3K, induces autophagic cell death through disruption of the glycolysis pathway in ovarian cancer cells, Int. J. Biol. Sci. 17 (2021) 1895–1908.
[23] M. Apostolidi, et al., Targeting pyruvate kinase M2 phosphorylation reverses aggressive cancer phenotypes, Cancer Res. 81 (2021) 4346–4359.
[24] Y. Zhou, et al., Benserazide is a novel inhibitor targeting PKM2 for melanoma treatment, Int. J. Cancer 147 (2020) 139–151.
[25] J. Chen, et al., Shikonin and its analogs inhibit cancer cell glycolysis by targeting tumor pyruvate kinase-M2, Oncogene 30 (2011) 4297–4306.
[26] X. Ning, et al., Discovery of novel naphthoquinone derivatives as inhibitors of the tumor cell specific M2 isoform of pyruvate kinase, Eur. J. Med. Chem. 138 (2017) 343–352.
[27] X. Wang, F. Zhang, X.-R. Wu, Inhibition of pyruvate kinase M2 markedly reduces chemoresistance of advanced bladder cancer to cisplatin, Sci. Rep. 7 (2017), 45983.
[28] X. Ning, et al., Synthesis and antitumor activity of novel 2, 3-didithiocarbamate substituted naphthoquinones as inhibitors of pyruvate kinase M2 isoform, J. Enzym. Inhib. Med. Chem. 33 (2018) 126–129.
[29] L.F. García-Alles, B. Erni, Synthesis of phosphoenol pyruvate (PEP) analogues and evaluation as inhibitors of PEP-utilizing enzymes, Eur. J. Biochem. 269 (2002) 3226–3236.
[30] J.J. Chen, L.N. Schmucker, D.P. Visco, Virtual high-throughput screens identifying hPK-M2 inhibitors: exploration of model extrapolation, Comput. Biol. Chem. 78 (2019) 317–329.
[31] K. Vanommeslaeghe, et al., CHARMM general force field: a force field for drug-like molecules compatible with the CHARMM all-atom additive biological force fields, J. Comput. Chem. 31 (2010) 671–690.
[32] J. Huang, A.D. MacKerell, CHARMM36 all-atom additive protein force field: validation based on comparison to NMR data, J. Comput. Chem. 34 (2013) 2135–2145.
[33] M.H.M. Olsson, C.R. Søndergaard, M. Rostkowski, J.H. Jensen, PROPKA3: consistent treatment of internal and surface residues in empirical pK predictions, J. Chem. Theor. Comput. 7 (2011) 525–537.
[34] E. Boedtkjer, S.F. Pedersen, The acidic tumor microenvironment as a driver of cancer, Annu. Rev. Physiol. 82 (2020) 103–126.
[35] P. Swietach, What is pH regulation, and why do cancer cells need it? Cancer Metastasis Rev. 38 (2019) 5–15.
[36] T.J. Dolinsky, J.E. Nielsen, J.A. McCammon, N.A. Baker, PDB2PQR: an automated pipeline for the setup of Poisson-Boltzmann electrostatics calculations, Nucleic Acids Res. 32 (2004) W665–W667.
[37] S. Doerr, M.J. Harvey, F. Noé, De Fabritiis, G. Htmd, High-Throughput molecular dynamics for molecular discovery, J. Chem. Theor. Comput. 12 (2016) 1845–1852.
[38] W. Humphrey, A. Dalke, K. Schulten, VMD: visual molecular dynamics, J. Mol. Graph. 14 (33–8) (1996) 27.
[39] M.J. Harvey, G. Giupponi, G.D. Fabritiis, ACEMD: accelerating biomolecular dynamics in the microsecond time scale, J. Chem. Theor. Comput. 5 (2009) 1632–1639.
[40] E.F. Pettersen, et al., UCSF Chimera—a visualization system for exploratory research and analysis, J. Comput. Chem. 25 (2004) 1605–1612.
[41] G. Xiong, et al., ADMETlab 2.0: an integrated online platform for accurate and comprehensive predictions of ADMET properties, Nucleic Acids Res. 49 (2021) W5–W14.
[42] G. Landrum, et al., Rdkit/Rdkit: 2020_03_1 (Q1 2020) Release, Zenodo, 2020, https://doi.org/10.5281/zenodo.3732262.
[43] rdkit.Chem.rdMolDescriptors module — the RDKit 2022.03.1 documentation. https://www.rdkit.org/docs/source/rdkit.Chem.rdMolDescriptors.html#rdkit.Chem.rdMolDescriptors.GetMorganFingerprint.
[44] J. Eberhardt, D. Santos-Martins, A.F. Tillack, S. Forli, Autodock vina 1.2.0: new docking methods, expanded force field, and python bindings, J. Chem. Inf. Model. 61 (2021) 3891–3898.
[45] O. Trott, A.J. Olson, AutoDock Vina: improving the speed and accuracy of docking with a new scoring function, efficient optimization, and multithreading, J. Comput. Chem. 31 (2010) 455–461.
[46] K. Vanommeslaeghe, A.D. MacKerell, Automation of the CHARMM General Force Field (CGenFF) I: bond perception and atom typing, J. Chem. Inf. Model. 52 (2012) 3144–3154.
[47] K. Vanommeslaeghe, E.P. Raman, A.D. MacKerell, Automation of the CHARMM General Force Field (CGenFF) II: assignment of bonded parameters and partial atomic charges, J. Chem. Inf. Model. 52 (2012) 3155–3168.
[48] J. Wang, W. Wang, P.A. Kollman, D.A. Case, Antechamber: an accessory software package for molecular mechanical calculations, J. Am. Chem. Soc. 222 (2001).
[49] A. Frisch, Gaussian 09w Reference, 2009, p. 25. Wallingford, USA.
[50] T.H. Duffy, T. Nowak, Stereoselectivity of interaction of phosphoenolpyruvate analogues with various phosphoenolpyruvate-utilizing enzymes, Biochemistry 23 (1984) 661–670.
[51] W.L. Jorgensen, J. Chandrasekhar, J.D. Madura, R.W. Impey, M.L. Klein, Comparison of simple potential functions for simulating liquid water, J. Chem. Phys. 79 (1983) 926.
[52] H.J.C. Berendsen, J.P.M. Postma, W.F. van Gunsteren, A. DiNola, J.R. Haak, Molecular dynamics with coupling to an external bath, J. Chem. Phys. 81 (1984) 3684.
[53] R.J. Loncharich, B.R. Brooks, R.W. Pastor, Langevin dynamics of peptides: the frictional dependence of isomerization rates of N-acetylalanyl-N'-methylamide, Biopolymers 32 (1992) 523–535.
[54] C.W. Hopkins, S. Le Grand, R.C. Walker, A.E. Roitberg, Long-time-step molecular dynamics through hydrogen mass repartitioning, J. Chem. Theor. Comput. 11 (2015) 1864–1874.
[55] U. Essmann, et al., A smooth particle mesh Ewald method, J. Chem. Phys. 103 (1995) 8577.
[56] R.T. McGibbon, et al., Mdtraj: a modern open library for the analysis of molecular dynamics trajectories, Biophys. J. 109 (2015) 1528–1532.
[57] B.R. Miller, et al., MMPBSA.py: an efficient program for end-state free energy calculations, J. Chem. Theor. Comput. 8 (2012) 3314–3321.
[58] E. Wang, et al., End-point binding free energy calculation with MM/PBSA and MM/GBSA: strategies and applications in drug design, Chem. Rev. 119 (2019) 9478–9508.
[59] S. Genheden, U. Ryde, The MM/PBSA and MM/GBSA methods to estimate ligand-binding affinities, Expet Opin. Drug Discov. 10 (2015) 449–461.
[60] K.A. Donovan, et al., Conformational dynamics and allostery in pyruvate kinase, J. Biol. Chem. 291 (2016) 9244–9256.
[61] T.M. Larsen, M.M. Benning, I. Rayment, G.H. Reed, Structure of the bis(Mg2+)-ATP-oxalate complex of the rabbit muscle pyruvate kinase at 2.1 A resolution: ATP binding over a barrel, Biochemistry 37 (1998) 6247–6255.
[62] H. Muirhead, et al., The structure of cat muscle pyruvate kinase, EMBO J. 5 (1986) 475–481.
[63] J. Liu, J.A. Peliska, M.H. O'Leary, Synthesis and study of (Z)-3-chlorophosphoenolpyruvate, Arch. Biochem. Biophys. 277 (1990) 143–148.
[64] J.A. Peliska, M.H. O'Leary, Sulfuryl transfer catalyzed by pyruvate kinase, Biochemistry 28 (1989) 1604–1611.
[65] S. Safari, M. Motavaf, S.A. Seyed Siamdoust, S.M. Alavian, Hepatotoxicity of halogenated inhalational anesthetics, Iran. Red Crescent Med. J. 16 (2014), e20153.
[66] Y. Wang, X.-X. Ming, C.-P. Zhang, Fluorine-containing inhalation anesthetics: chemistry, properties and pharmacology, Curr. Med. Chem. 27 (2020) 5599–5652.